

# Chapter 22

## Multilayer Zone Plates for Hard X-ray Imaging



Markus Osterhoff and Hans-Ulrich Krebs

**Abstract** This chapter reviews progress both in the fabrication of multilayer zone plate optics for focusing X-rays, as well as in imaging experiments using these optics. The fabrication based on pulsed laser deposition is accompanied by analytical and numerical treatment of X-ray propagation to control volume diffraction effects. On the imaging side, different schemes are presented; these include scanning-scattering with focused X-rays, holography, as well as recent advances in lens-enhanced phase-reconstruction.

### 22.1 From Focusing to Imaging

In this chapter we review progress on hard X-ray imaging methods using Multilayer Zone Plate (MZP) optics. First, we have developed Multilayer Laue Lenses (MLLs), as a means to one-dimensionally focus soft X-rays produced at table-top laser-driven plasma sources, see also Chap. 21. Focusing experiments using a depth graded MLL consisting of Ti/ZrO<sub>2</sub> layer were performed with the table-top soft X-ray source at a wavelength of 2.88 nm, achieving a focal spot size of 280 nm [1, 2].

Then, first focusing experiments using MLLs and MZPs have demonstrated that two-dimensional focusing of hard X-rays (7.9 and 13.8 keV) is possible at 3rd generation synchrotron radiation sources. For technical reasons, only optics with rather small aperture sizes have been fabricated in Göttingen. To compensate, pre-focusing optics (Kirkpatrick-Baez mirrors, KBs, or Compound Refractive Lenses, CRLs) were used to increase the flux density on the zone plates. In the first experiment, an MLL with a height of 401 nm was illuminated by a pre-focused KB mirror beam. From

---

M. Osterhoff (✉)

Institute for X-ray Physics, Universität Göttingen, Friedrich-Hund-Platz 1,  
37077 Göttingen, Germany  
e-mail: [mosterh1@gwdg.de](mailto:mosterh1@gwdg.de)

H.-U. Krebs

Institute for Material Physics, Universität Göttingen, Friedrich-Hund-Platz 1,  
37077 Göttingen, Germany

© The Author(s) 2020

T. Salditt et al. (eds.), *Nanoscale Photonic Imaging*, Topics in Applied Physics 134,  
[https://doi.org/10.1007/978-3-030-34413-9\\_22](https://doi.org/10.1007/978-3-030-34413-9_22)

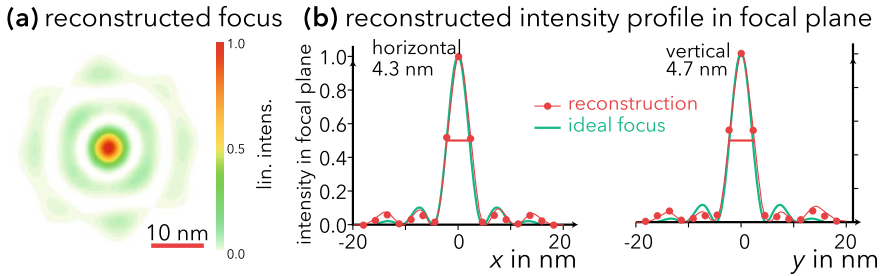


**Fig. 22.1** Reconstructed intensity profile of an MZP focus: **a** two-dimensional rendering on linear colour scale, **b** one-dimensional intensity cuts with Gaussian fit. The full width at half maximum is determined to  $4.3 \text{ nm} \times 4.7 \text{ nm}$ . Adapted from [4]

far-field measurements, a focal spot size of  $6.8 \text{ nm}$  (FWHM) was reconstructed at  $13.8 \text{ keV}$  photon energy [3].

Later, a two-dimensional hard X-ray spot was achieved. While two MLL optics were successfully crossed, the fabrication of a round MZP optic succeeded, too: A depth-graded circular W/Si multilayer was deposited onto a rotating W wire. In contrast to lithographic fabrication, virtually unlimited aspect ratios of outer-most zone width (here: down to  $5 \text{ nm}$ ) and optical thickness (here: length of straight sections of the wire, usually several hundred micrometres) are possible. In a first experiment—again with the nano-focusing optic placed in the KB beam—an unprecedented focal spot size of  $4.3 \text{ nm} \times 4.7 \text{ nm}$  was reconstructed (see Fig. 22.1) [4].

Backed by these achievements, the fabrication of round MZPs was improved significantly. In the following, we will concentrate on research dedicated to further optimise the lenses, and apply them for new hard X-ray imaging schemes [5]. First, we will cover the advanced design and improved fabrication; then we will review different experiments performed at synchrotron setups, and present results obtained during those imaging experiments.

Preliminary imaging experiments could be performed, see Fig. 22.2a for a scanning-SAXS measurement on a Siemens star [5]. In Fig. 22.2b, c, multi-order images of semiconductor nanowires are shown. Scanning experiments without an Order Sorting Aperture yield information both from the holographic  $-1\text{st}$  order and the focused  $+1\text{st}$  order. Figure 22.2b shows an overview hologram of nanowires; the information in the centre of the image is missing due to a beamstop. But a high-resolution scanning-SAXS measurement in differential phase contrast mode of a nanowire on an electrical contact is shown in Fig. 22.2c. Both images are extracted from the same dataset.

For a detailed description of Fresnel and Multilayer Zone Plates, see Chap. 3.

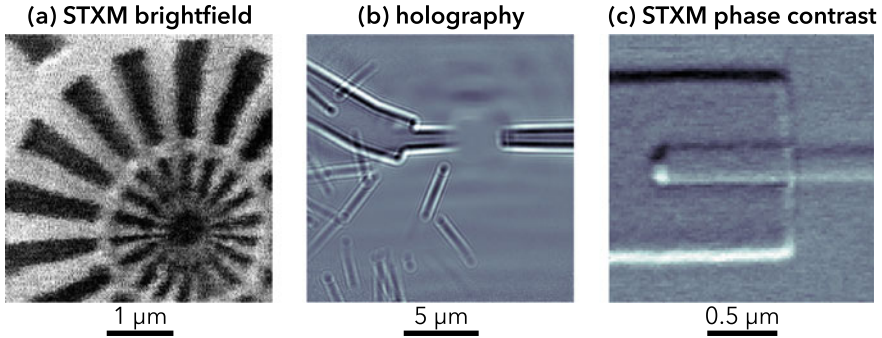


**Fig. 22.2** **a** First MZP-based STXM brightfield scan of a Siemens star test pattern, adapted from [5]. The smallest features of 50 nm could not be resolved due to vibrations of the early experimental setups. **b** Holographic image obtained the diverging –1st order, after overlaying of shifted sample positions. The sample consists of semiconductor nano-wires [6] and electrical contacts. The centre is not visible in this image due to a beamstop; **c** but in scanning-SAXS mode, here differential phase contrast. The image has been extracted using a “software-OSA” from the same measurement as the hologram, and shows a single nano-wire lying on an electrical contact. The tip of the nano-wire consists of a Au sphere

## 22.2 Let There be an Ideal World

In this section we show simulation results for “perfect” zone plates to assess the best case scenario and to devise new measurement techniques.

Optically thin Fresnel Zone Plates (FZPs) are constructed via the Zone Plate Law, cf. Sect. 3.5. To model thin FZPs, an incoming wave-field can be multiplied pixel-wise with a complex-valued transmission function. For thick Multilayer Zone Plates, however, this approximation cannot be met. Usually, wave-optical propagation modelling through the structure has to be applied, if

$$F := \frac{(\Delta r_N)^2}{\lambda t} \lesssim 1, \tag{22.1}$$

with outer-most zone thickness  $\Delta r_N$ , wavelength  $\lambda$ , and optical thickness  $t$ . For  $\Delta r_N = 5 \text{ nm}$  and  $\lambda = 1 \text{ \AA}$ , the geometrical approximation becomes invalid for  $t \gtrsim 250 \text{ nm}$ .

The “imprint” of an infinitely thin zone plate on an impinging wave field  $\psi(x, y)$  is usually described by a complex-valued transmission function  $\tau(x, y)$ ; the outgoing field can then be propagated to e.g. the focal plane using the Fresnel-Kirchoff integral. For longitudinally extended objects, multi-slice approaches with various propagators are used; these alternate between numerical free-space propagation and transmission functions for “short” propagation distances with  $F \gg 1$  instead of (22.1). In the general case,  $\tau(x, y, z)$  can also change along the optical axis, so volume zone plates

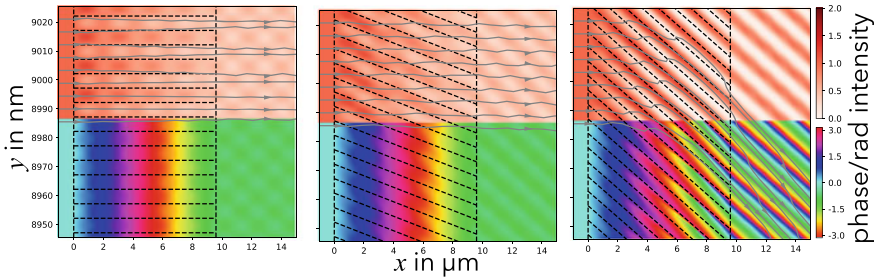


**Fig. 22.3** Intensity (top) and phase (bottom) simulated inside outermost zones of a flat (left), tilted (centre), and wedged (right) MZP; the grey arrows show the direction of the Poynting vector field, i.e. the “flow” of intensity. In the flat geometry, a “beating mode structure” known from array waveguides emerges after only  $1\ \mu\text{m}$ , and the Poynting vectors are almost unaltered in direction, and also the phase fronts are almost perpendicular to the incoming beam direction; hence, the focusing efficiency is very limited. In the tilted case, the impinging field is coupled into the channels for about  $2\ \mu\text{m}$ , and a focusing effect becomes visible in the outgoing intensity pattern. But only for the wedged case also the Poynting vectors align in the direction of the desired focal spot

with tapering can be described. Here, we have mostly made use of the paraxial wave equation described in Chap. 2.

Such tapering becomes important at higher X-ray energies (i.e., long devices) and smaller zones (i.e., smaller focus). This is shown in the simulation shown in Fig. 22.3, where three layouts of MZPs are compared. The three columns show the intensity (top) and phase (bottom) for a flat MZP (left), a tilted MZP (centre) and a wedged MZP (right). Dashed lines show the nano-focusing zones on a scale of  $5\ \text{nm}$ , over an optical thickness of about  $9.8\ \mu\text{m}$ .

In both flat and tilted case, the phase fronts are almost flat and perpendicular to the optical axis. Also, a “mode beating” effect known from array waveguides can be seen in the intensity patterns. In the flat case, this beating starts at around  $1\ \mu\text{m}$ , while for the tilted case the incoming wave is coupled for about  $2\ \mu\text{m}$  into the “channels”. In the flat case, the outgoing wave field reproduces the “checker board” pattern; the tilted geometry, on the other hand, shows stripes directed towards the focus, promising enhanced efficiency.

The grey arrows show the local direction of the Poynting vector field. In both cases, this field points almost parallel to the optical axis. Since the Poynting vectors locally measures the energy flow, this shows that the focusing efficiency into the  $+1\text{st}$  order is rather small.

For the wedged case, on the other hand, the Poynting vectors are bent towards the focal point.

## 22.3 Back to the Real World: Fabrication Challenges

Now we will leave the neat and clean simulations to “dive into the real world”.

In this section we briefly review a particular fabrication technique for Multilayer Zone Plates. Firstly, by Pulsed Laser Deposition (PLD), a rotating glass fibre is coated with alternating layers; secondly, the final MZP is sliced out using a Focused Ion Beam (FIB) device.

First, a depth graded multilayer was grown on a wire according to the Zone Plate Law by PLD. Then, the MZP was fabricated by cutting a slice out of the multilayer with desired optical depth by FIB. The MZP was positioned onto a W tip, which can be used as sample holder during hard X-ray focusing. For the first focusing experiments, the MZP was illuminated by a pre-focused X-ray beam at the coherence beamline P10 of the PETRA III synchrotron. Later on, a sample is either put into the MZP focus (scanning-SAXS/scanning-WAXS) or into the MZP defocus (holography) for imaging experiments.

### 22.3.1 Pulsed Laser Deposition

As a thin film sputtering technique, PLD allows the deposition of multilayer structures with reliable layer thicknesses just in the range suitable for hard X-ray focusing optics. One advantage over other sputtering techniques originates in the high energetic bombardment: New particles enter the structure and increase the mobility. In the end, this “self-healing” property decreases roughness and tends towards cylindrical layers even on a slightly elliptically wire.

The thin film deposition was realized by a computer controlled KrF excimer laser (wavelength of 248 nm, pulse duration of 30 ns, repetition rate of 10 Hz). The laser beam was focused onto the different targets in ultrahigh vacuum of about  $10^{-8}$  mbar. The targets were moved constantly following an algorithm that allows uniform ablation from different directions. The films were grown at room temperature at a target-to-substrate distance of 65 mm. By both changing the distance of the focusing lens to the target and the laser energy, the laser fluence was controlled in a range of  $1-5 \text{ J/cm}^2$  [7].

Different material combinations have been tested during this Collaborative Research Centre. We will present the results of W/Si, W/ZrO<sub>2</sub>, and the final combination Ta<sub>2</sub>O<sub>5</sub>/ZrO<sub>2</sub> further [8–10].

### 22.3.2 FIB Processing

Within the FIB-facility (Nova NanoLab600, FEI), for further protection an additional layer of Pt is deposited onto the multilayer by electron beam deposition. Then, the

specimen is cut by a 30 kV Ga<sup>+</sup>-ion beam (using a current of about 1 nA) close to the region, where the wire had its desired diameter. A piece of the coated wire is attached to a thin W-micromanipulator with electron and ion-beam deposited Pt and transferred onto the final lens holder, e.g. a W tip prepared beforehand. Afterwards, the micromanipulator gets cut off and is drawn back, leaving the coated wire on the tip. Finally, the lens is shaped and polished by less energetic Ga<sup>+</sup>-ions (5 kV, ca. 30 pA) down to the desired optical thickness, usually around 6 μm; for the high-energy experiment, an MZP of 30 μm optical thickness has been prepared.

### 22.3.3 From MLL to MZP

For the table-top soft X-ray microscope developed in project C04, one-dimensional Multilayer Laue Lenses (MLLs) have been manufactured. Other than round MZPs, these consist of parallel films on a flat substrate. It was found that PLD also works on curved substrates, and hence two-dimensionally focusing devices can be manufactured. To this end, a rotation motor was incorporated into the PLD vacuum chamber; the alternating layers are then deposited onto a thin wire while the latter rotates around its axis.

Geometrically, the layer thickness is reduced by a factor of  $\pi$  for the same number of pulses. Experimentally, however, transfer factors of  $TF \approx 3.8$  (Ta<sub>2</sub>O<sub>5</sub>) and  $TF \approx 3.3$  (ZrO<sub>2</sub>) were found. The deviation from the geometrical  $TF_{\text{geo}} = \pi$  can be explained by resputtering and reflection during the deposition on tilted substrates. From experimental data it is found that the dependance of the deposition rate on the angle  $\varphi$  to the substrate varies more strongly than the expected  $\cos \varphi$ . This behaviour could be reproduced using SDTrimSP simulations [8].

Note that due to aging of the target materials the deposition rates also change in time. This can be compensated by changing the number of pulses accordingly.

Glass wires for the MZP were prepared in a heat-and-pull process using standard glass fibres [9, 11]. The core wire of the Ta<sub>2</sub>O<sub>5</sub>/ZrO<sub>2</sub> MZP was prepared using a Sutter Instruments flaming/brown micropipette puller system P1000. With this technique it has become possible to prepare round glass fibres of suitable diameters between 1 μm and 2 μm. Within our parameters, this corresponds to the first about ten zones of the Zone Plate Law that are missing. In addition, it is possible to draw tapered fibres with an opening angle of few degree, see Fig. 22.4a.

### 22.3.4 Material and Parameter Studies

During this Collaborative Research Centre, different material combinations (W/Si, Ta<sub>2</sub>O<sub>5</sub>/Si, and Ta<sub>2</sub>O<sub>5</sub>/ZrO<sub>2</sub>) have been tested, and the PLD parameters (mainly the laser energy, or flux density) have been optimised.

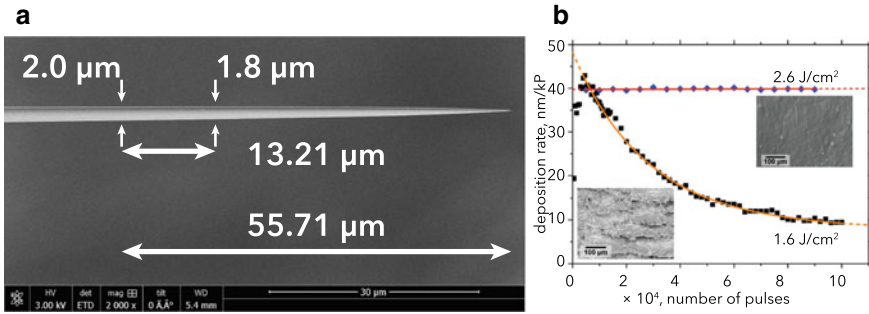


**Fig. 22.4** **a** SEM image of a tapered glass fibre, prior to coating: both tapering angle (here about 0.9°) and diameter (here around 2 μm can be tweaked during the pulling process). **b** In situ deposition rate measurements during target aging for Ta<sub>2</sub>O<sub>5</sub>. For a laser fluence of 1.6 J/cm<sup>2</sup> (black), plate like structures are formed on the target surface leading to a strong decrease of the deposition rate at higher pulse numbers. In contrast, the deposition rate becomes extraordinary stable at 2.6 J/cm<sup>2</sup> (blue). The SEM pictures show the corresponding target morphologies after 10<sup>5</sup> pulses. From [8]

When calculating the number of pulses necessary to fulfil the Zone Plate Law, the deposition rate has to be known. The rate depends on the material and laser energy; it was also found that during the deposition process, the rate changes on short and long time scales due to target aging. Deposition rates have been obtained from reflectivity measurements on coated flat substrates. The time-dependent rates are then used by the control software to calculate the number of pulses for the individual layers.

Especially the W/Si system suffered from strongly varying deposition rates. With increasing number of laser pulses, in both cases the deposition rate first strongly rises and then monotonously decreases again. The very early stages of target aging depend on the initial surface topography. On longer time scales, the deposition rate decreases exponentially with the number of pulses; this is attributed to further surface roughening (for W) and to cone formation (for Si). Also, the W/Si system suffers from some limitations due to droplet formation during ablation of Si. The laser fluence was tuned to 1.7 J/cm<sup>2</sup> to reduce the number of droplets; still about 400 droplets per mm<sup>2</sup> are found on a 10 nm layer.

To circumvent droplet formation, Si was replaced by ZrO<sub>2</sub>, which also offers a large phase shift for X-rays when combined with W. In contrast to Si, the surface of ZrO<sub>2</sub> targets remains relatively smooth at a laser fluence of 1.8 J/cm<sup>2</sup>, and droplet formation is almost completely avoided. Furthermore, the deposition rate of ZrO<sub>2</sub> is about five times higher than for Si (about 45 nm per 10<sup>3</sup> pulses) and remains much more stable. In contrast to W/Si, no enhanced resputtering is observed at the interfaces of planar W/ZrO<sub>2</sub> multilayers by in situ rate measurements, even at increased laser fluence on the ZrO<sub>2</sub> target.

To increase the deposition rates, W was replaced by Ta<sub>2</sub>O<sub>5</sub>; it was found that for a laser fluence of 2.6 J/cm<sup>2</sup>, the deposition rate becomes extraordinary stable and gives ideal conditions for the deposition of both thin and thick films. The development of the Ta<sub>2</sub>O<sub>5</sub> deposition rates for two fluences is shown in Fig. 22.4b.

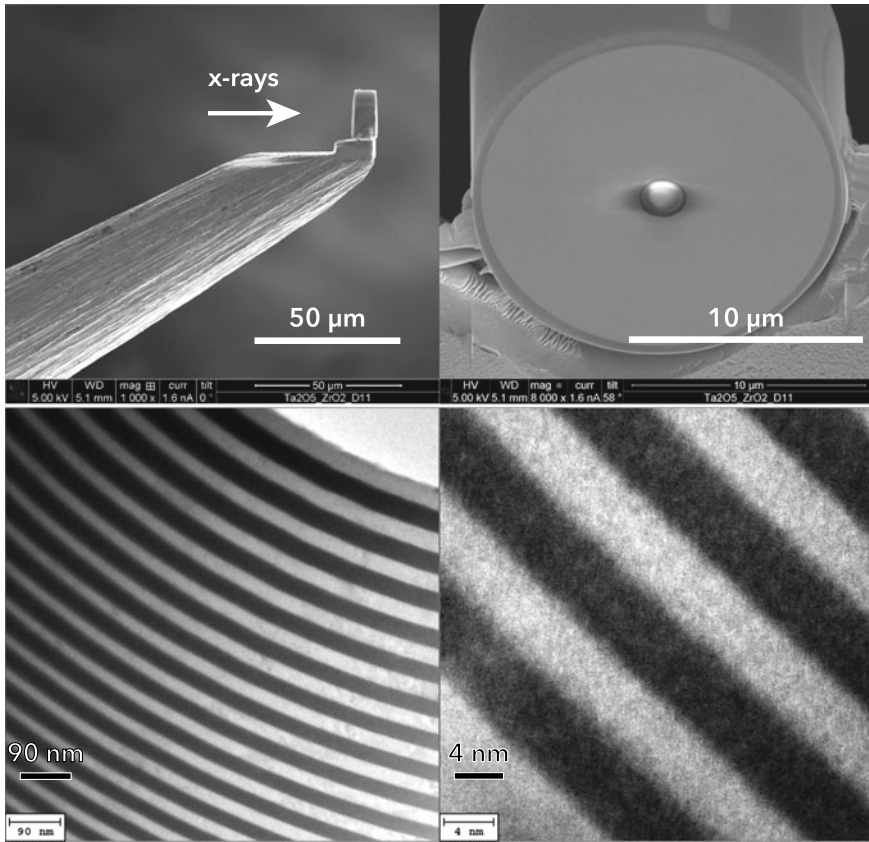


**Fig. 22.5** SEM images (top) and TEM images (bottom) of “D13”, an MZP with outermost zone width of 5 nm and a diameter of 16  $\mu\text{m}$ . The optical thickness (top left) of 7  $\mu\text{m}$  is designed for an X-ray energy of 14 keV. Adapted from [9]

Since the deposition rates of both materials were sufficiently high and did not change significantly over time, multilayers with precise layer thicknesses and larger overall thickness of 1.2  $\mu\text{m}$  could be deposited onto the glass wire, while almost no droplet formation occurred at the same time.

Recently, MZPs with a diameter of 16  $\mu\text{m}$ , outer-most zones down to 5 nm, and optical thicknesses of up to 7  $\mu\text{m}$  have been built and successfully used in X-ray experiments; see Fig. 22.5 for SEM and TEM images.



### 22.3.5 *Summary*

Due to high and almost constant deposition rates, minimization of resputtering, sharp multilayer interfaces, and low transformation factors,  $\text{Ta}_2\text{O}_5/\text{ZrO}_2$  is a very promising multilayer system for the fabrication of high quality lenses for hard X-rays by the combination of PLD and FIB.

## 22.4 The World of Synchrotron Instrumentation

Here we briefly describe the basic setup used at synchrotron radiation facilities for the imaging experiments presented later on. Most measurements were carried out using the GINIX end-station of the P10 beamline at the PETRA III synchrotron (DESY, Hamburg). The high-energy experiment at 60 keV up to above 100 keV was performed at the ID31 beamline of the European Synchrotron Radiation Facility (ESRF; Grenoble, France); recently, a ptychographic measurement was successfully carried out at the PtyNAMi setup of the P06 beamline at PETRA III.

### 22.4.1 *Hard X-rays Near 14 keV*

Most experiments were carried out using the versatile Göttingen Instrument for Nano-Imaging with X-rays (GINIX) at the P10 coherence beamline of PETRA III [12]. From the undulator radiation, a monochromatic beam around 8.0 or 13.8 keV is filtered by either a double-crystal Si(111) monochromator, or by a more stable channel-cut monochromator. Then, with Compound Refractive Lenses (CRLs), the X-ray beam is pre-shaped onto the MZP and the sample.

During first alignment of the zone plate, the CRLs are moved out of the beam. Alignment of the MZP-tip/tilt angles is eased when illuminated by a large beam of around 200  $\mu\text{m}$  diameter. For the MZP-based measurements, the CRL beam is usually set to a beam size of approximately 30  $\mu\text{m}$ , so an MZP with diameter of 16  $\mu\text{m}$  is illuminated homogeneously. It was found during the scanning SAXS/WAXS measurements, that combining the ultra-small focal spot of the MZP with a 2  $\mu\text{m}$  CRL beam and a lithographic FZP of 30 nm zone width enables a profitable zoom-in capability. Since all three kinds of optics are in-line (without lateral shifts), features of the sample can be measured at different sequential resolution levels.

For the success of these experiments, close collaboration with Michael Sprung, beam line responsible for the P10 at DESY, Hamburg, and Tim Salditt, project leader of C01, was crucial; we thank Michael, Tim, and their teams for outstanding support.

### 22.4.2 *High Energies: From 60 to 101 keV*

Opposed to Fresnel Zone Plates, which are traditionally fabricated using lithography and hence achieve only small aspect ratios, Multilayer Zone Plates are a promising optic to focus even higher X-ray energies. The regime above 30 keV is usually attributed to Compound Refractive Lenses; here, we show that also MZPs can be used to focus photon energies from 60 to 100 keV. The proof of principle experiments were carried out at the high energy beam line ID 31 at the European Synchrotron Radiation Facility (ESRF) in Grenoble, France.

The MZP setup (see next subsection for more details) was integrated into the HEMD setup (High Energy Microdiffraction Instrument). This X-ray diffractometer is used to study buried interfaces; micro-focused X-ray beams of high energies can penetrate even metallic specimens. Scattering from buried interfaces (Reflectivity), hidden nano-scaled particles (SAXS), or packaged crystallites can be investigated. As detector, a Pilatus 2M single-photon counting pixelated hybrid detector with CdTe sensor material is used.

For the experiment, an MZP with a diameter of 8  $\mu\text{m}$  and smallest zones of 10 nm was fabricated using PLD; with the FIB, a thick slice of 30  $\mu\text{m}$  was cut out. This length provides optimal phase shift at 60 keV.

We report on our experiment in the Imaging section further below [10].

### 22.4.3 *Sampler Scanner*

In an early phase of the project, we learned that the versatile approach of the GINIX setup poses severe limits on resolution once the 10 nm region is targeted. To minimise vibrations and drift, a new sample tower was designed and commissioned. Only the most essential degrees of freedom for the imaging experiments are included.

For the MZP, three translational stages based on the Piezo stick-slip principle by SmarAct GmbH (Oldenburg, Germany) are used for lateral alignment; the vertical  $z$ -movements are accomplished by an inclined linear positioner and an additional free-moving guideway to increase stability. On top, horizontal movements are facilitated by one positioner plus one guideway (lateral  $y$ -direction) and by one positioner of increased stability (longitudinal  $x$ -direction). Travel ranges are 10 mm in  $z$  (vertical), and  $>40$  mm in  $x$  and  $y$  (horizontal). The  $x$ -motor then has an adjustable mount position for an FZP optic, and holds a tip/tilt motor for the MZP optic. This tip/tilt is adapted from a motorised optical mount with stick-slip motors in open-loop mode. The maximum angles are  $\pm 5^\circ$ . A custom-built encoder based on a two-dimensional Position Sensitive Detector (SEEPOS PSD Signal Process System with 2L45\_MH02 sensor; SiTek Electro Optics, Partille, Sweden) is being commissioned to improve the angular motorisation.

For the sample, three translations by Physik Instrumente (PI GmbH, Karlsruhe, Germany) are used for coarse alignment. For  $x$  and  $y$ , a PILine piezo ultrasonic drive

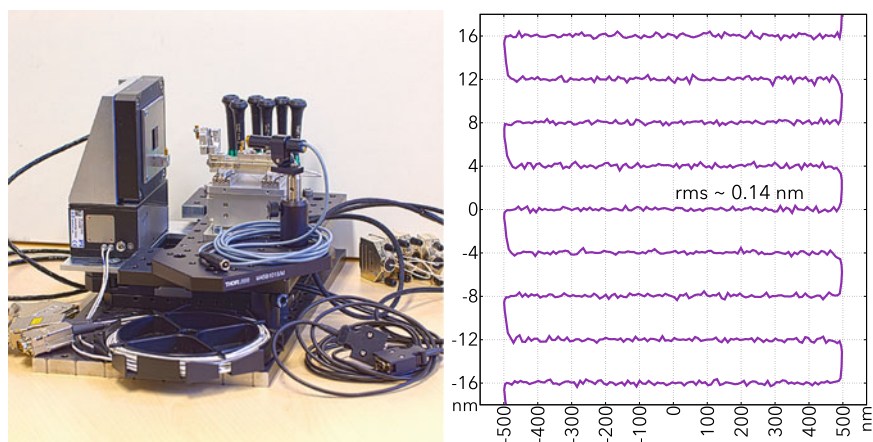


**Fig. 22.6** Photograph of the Multilayer Zone Plate sample scanner (left) and encoder values recorded during a fast two-dimensional scan (right). The MZP is mounted on a tip-tilt stage with large translational stages by SmarAct; the sample is then coarsely aligned by three translations, and can be raster-scanned using a two-dimensional piezo stage by PI Physik Instrumente. According to encoder values, the positional accuracy of the continuous scan is better than  $2 \text{ \AA}$

of large area (model M-686) is used as base; a vertical NEXACT Piezo stepping drive (model N-765) with a high load capacity of 25 N is mounted on top. Travel ranges are 25 mm in  $x$  and  $y$ , and 6.5 mm in  $z$ . On top of the alignment motors is a vertically mounted Piezo scanner of high stiffness with a clear aperture of 50 mm edge length (model P-733). The built-in capacitive sensors show an r.m.s. noise of better than 0.2 nm. The maximum travel range is  $30 \mu\text{m}$ ; line scan speeds of 100 Hz and more are possible at reduced travel range.

All translational stages employ optical encoders with nanometre resolution. The non-linear, but reproducible movements of the tip/tilt stage have been characterised and adjusted in software by fourth order polynomials (Fig. 22.6).

The stage was designed for fast Scanning Transmission X-ray Microscopy (STXM) with new hybrid pixelated photon-counting detectors like the EigerX 4M (Dectris Inc., Baden-Daetwill, Switzerland). This particular detector is able to image at 750 Hz frame rate; each of the four million pixels has a full analog-digital processing chain to count single photon events. When configured for “fly scan mode” (continuous STXM), the Piezo moves a two-dimensional trajectory and starts a series of detector acquisitions via hardware trigger; a common scan consists of 255 lines with 255 detector frames each. In the fastest mode with 1.3 ms exposure times this is done in less than three minutes. This could be shortened further in bi-directional scanning mode [13, 14].

During fast scanning, inertial forces of the Piezo stage and sample holder have to be compensated by the mechanical system; otherwise, the MZP itself moves significantly, rendering the system unusable. We have measured the mechanical feedback from the sample part onto the optic part of the setup. For that, the movement of the

MZP holder has been measured interferometrically, and vibrations induced by both currently used and ultimate scanning parameters have been studied. It was obtained that the mechanical feedback is usually less than 0.1%; this means that during a STXM scan of 1,000 points, the MZP moves by less than one “pixel”. Hence, this mechanical feedback does not induce new non-linearities into the system.

For data analysis of large STXM scans, the dedicated “Heinzelmännchen” cluster is capable of analysing up to 3,000 frames per second [15, 16].

#### 22.4.4 Improvements of the GINIX Setup

The GINIX instrument at the P10 beamline at PETRA III was designed for waveguide based holography at resolution scales of about 100nm. With progress in optics fabrication (both for waveguides and for zone plates), this became a limiting factor in imaging. Together with project C01, several measures have been implemented to improve the stability. But first, the vibrations had to be quantified in a reliable manner. For that goal, two techniques have been applied. (i) Laser interferometry is able to measure the relative distance between two objects; this allows to quantify the absolute translational amplitude, but only relative between emitter and reflector. On the other hand, (ii) acceleration sensors (accelerometer 731-207 by Wilcoxon Research Inc., Meggitt PLC, Dorset, UK; including Dataq DI-155 data logger/Red Pitaya STEMLab) can measure absolute movements in space, but only the second time derivative. Numerical integration to extract the distance signal cannot reproduce slow and long-term drift-like movements. Note that both methods yield one-dimensional data.

After the implementation of vibration measurements, different strategies to improve the situation have been evaluated. We briefly discuss a few methods and share lessons learned.

**Active vibration isolation** using e.g. the *Nano Series* (Accurion GmbH, Göttingen) is a portable plug-in system that measures and actively damps vibrations in six degrees of freedom. We found that amplitudes of 50 nm and below are already “too good” for the system to work properly; instead, high frequencies were shifted to drift on the sub-second scale. Within the requirements of C01 and C12, the system did not work as desired.

**Passive vibration isolation** using a mechanical mass damper was implemented based on finite-element simulations modelling the vibrations. The principle is that an inert mass is accelerated by the vibrations, and the movements are subsequently dissipated by pushing a rubber absorber. During tuning of the resonance frequency, virtually no measurable effect could be seen; however, vibrations change significantly from night to day. It is assumed that the rubber absorber does not dissipate enough energy for very small amplitudes.

**Further attempts** include additional air springs, rubber mounts, and foams. Also, it has been tried to shift the resonance frequencies by additional masses on the breadboard. No measurable improvement of the vibrations could be achieved.

**High-resolution platforms** based on additional granite tables and combined sample towers with integrated mountings for optics. While the general flexible instrument of the GINIX is remained, high-resolution experiments are enabled by additional setups. For more details on the sample tower of project C12, see the previous subsection.

## 22.5 Imaging

In this section, we report on several imaging experiments. During the progress of project C12, many different imaging modalities have been implemented and tested for their suitability to study different samples in different geometries. Here, only a selection of results is presented.

### 22.5.1 Ptychography

During the second and at the beginning of the third funding period of our CRC, several attempts for a ptychographic reconstruction of the MZP focus were tried—unsuccessfully. Ptychography is a scanning technique that uses overlapping measurements to support both phase retrieval and the separation of wave-fields into illumination and sample scattering. Ultra-small beam sizes of MZPs on the order of sub-10 nm, however, introduce several problems, which were identified and subsequently resolved.

**Vibrations** on the order of 50 nm are a drawback of the flexibility of the GINIX setup. More details have been given in the previous section. First experiments suffered a lot; also because online-reconstruction was not possible during early stages of the project, visual feedback to steer the experiment was missing.

**Sampling issues** due to the diverging  $-1$ st diffractive orders rendered the reconstruction impossible. For ptychography to work correctly, the maximum beam size is bounded by  $\lambda R/\Delta$ , where  $R$  is the sample—detector distance and  $\Delta$  the detector's pixel size. With Pilatus detectors and hence  $\Delta = 172 \mu\text{m}$  in a distance of  $R = 5 \text{ m}$ , the illuminated area has to be smaller than about  $1 \mu\text{m}$  in diameter. The negative order of our MZP optics, however, illuminates a circle of more than  $30 \mu\text{m}$ .

#### 22.5.1.1 Results at the PtyNAMi Instrument

To overcome the sampling issue of the negative order, we have successfully introduced an OSA close to the focal spot during a beamtime at the PtyNAMi instrument of the P06 beamline (PETRA III, DESY Hamburg). Due to the short focal length of  $f \approx 1 \text{ mm}$ , the OSA needs to be positioned about  $200 \mu\text{m}$  upstream of the focus. Then, a Siemens star test pattern was moved from the downstream side close to the

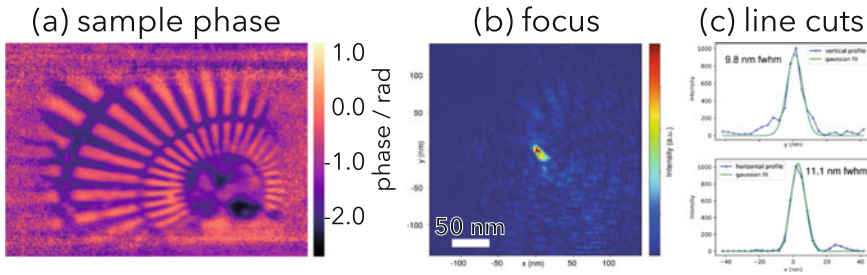


**Fig. 22.7** **a** Ptychographic phase reconstruction of a Siemens star test pattern, **b** shows the intensity of the X-ray nano focus on a linear colour map in the best focal plane, **c** shows horizontal and vertical line cuts, with Gaussian fits of about  $10 \text{ nm} \times 11 \text{ nm}$

focal region; after careful approaching, ptychographic scans could be performed. Results of the reconstruction are shown in Fig. 22.7. Figure 22.7a shows the reconstructed phase of the Siemens star; the smallest features of 50 nm are clearly resolved. Also damaged regions in the central part from an earlier experiment are visible. Figure 22.7b shows the intensity distribution in the best focal plane after numerical propagation; horizontal and vertical line cuts with Gaussian fits are shown in Fig. 22.7c. The FWHM of the focal spot size can be estimated to about 10 nm.

Note that the used MZP was not the “design cut” from the wire, and alignment could not be perfected during the ptychographic experiment during the allocated time slot. Nonetheless, this is the first successful ptychographic reconstruction of the MZP focus, indicating that resolution on the single-digit nanometre scale is in reach.

## 22.5.2 Holography and Scanning SAXS

Holography is a full-field imaging method, and the contrast is based on the local electron density inside the specimen and its imprint in the near-field intensity distribution. Scanning SAXS, on the other hand, is an imaging modality where sample or focused X-ray beam are scanned, and the contrast is extracted from far-field diffraction patterns and carries information about ordered structures inside the illuminated area [17–22]. For diffractive optics like Zone Plates, usually an order sorting aperture (OSA) is placed between sample and FZP. With a short focal length of  $\sim 1 \text{ mm}$  for the MZPs used here, the alignment of an OSA becomes impractical; hence, a “software OSA” has been used to extract multi-order holographic images from combined scanning-holography datasets. The scheme for each order is similar to the propagation-based imaging described in Chap. 2.

For sake of simplicity, we make use of the first diffractive orders,  $+1\text{st}$  and  $-1\text{st}$ ; with the sample placed in a defocus plane  $\Delta x \neq 0$ , the propagation distances are

$x_{+1} = \Delta x$  and  $x_{-1} = 2f + \Delta x$ ; with the detector placed at a position  $x_2$  from the MZP, the effective distances become

$$\tilde{x}_{+1} = \frac{\Delta x \times x_2}{\Delta x + x_2} \approx 0.1 \text{ mm}, \quad \tilde{x}_{-1} = \frac{(2f + \Delta x) \times x_2}{2f \Delta x + x_2} \approx 2.1 \text{ mm}.$$

For the numerical values, we have assumed a focal distance  $f = 1 \text{ mm}$ , a defocal distance  $\Delta x = 0.1 \text{ mm}$ , a detector distance  $x_2 = 5 \text{ m}$ , an X-ray wavelength  $\lambda = 1 \text{ \AA}$ , and a detector pixel size of  $p = 75 \text{ }\mu\text{m}$ .

The corresponding Fresnel numbers and magnifications are

$$F_{+1} = \frac{(p/M_{+1})^2}{\lambda \times x_2} \approx 4.5 \times 10^{-9}, \quad F_{-1} = \frac{(p/M_{-1})^2}{\lambda \times x_2} \approx 2.0 \times 10^{-6};$$

$$M_{+1} = \frac{\Delta x + x_2}{\Delta x} = 50,001 \times, \quad M_{-1} = \frac{2f + \Delta x + x_2}{2f + \Delta x} \approx 2382 \times .$$

When the sample is laterally scanned in the defocus plane  $\Delta x$ , both holograms “move” with different velocities in the detector plane; by a simple re-arranging of the pixelated intensity values according to the magnifications  $M_{\pm 1}$ , two scaled holograms can be obtained. Also, an “average flat-field” can be extracted from the measurement.

For  $\Delta x \rightarrow 0 \Rightarrow F_{+1} \rightarrow \infty$ , and the +1st signal approaches a traditional Scanning X-ray Transmission Microscopy (STXM) contrast; in first order, differential phase contrast maps can be deduced from tracking the centred moment of the intensity distribution:

$$\varphi'(y) = k \sin \vartheta = \frac{2\pi}{\lambda} \sin \tan^{-1} \frac{\int I(y) y \, dy}{\int I(y) \, dy}.$$

Combing these imaging modalities of the 5 nm MZP with a “traditional” (i.e., lithographically produced) FZP with an outermost zone width of 30 nm, and a compound refractive lenses (CRL) optics with a focus size of about  $2 \text{ }\mu\text{m}$ , multi-scale imaging with a zoom-in capability has been explored. The different optics and field-of-views are shown in Table 22.1.

A phase-reconstruction using the relaxed averaged alternating reflection (RAAR) algorithm has been carried out on the  $-1$ st order hologram of semiconductor nanowires (for raw hologram, see Fig. 22.2). An overall view is shown in Fig. 22.8a, while Fig. 22.8b shows a zoom-in on a single nanowire. These reconstructions stem from the holographic dataset in Fig. 22.2b; Fig. 22.2 shows a close-up of the (here invisible) nanowire lying on an electrical contact in (vertical) differential phase contrast mode.

**Table 22.1** For multi-scale imaging, different optical illuminations and measuring schemes are combined, with a decreasing field of view and increasing (ideal-case) resolution. The Compound Refractive Lenses (CRL) are from the P10 beamline, DESY Hamburg; the Fresnel Zone Plate (FZP) was generously provided by Christian David, PSI (CH); the Multilayer Zone Plate (MZP) is “D13” from the C12 project

Optical setup	Measuring scheme	Field of view	Resolution limit
Parallel beam	Holography, SAXS, WAXS	$\geq 200 \mu\text{m}$	Detector pixel size
MZP, -1st	Holography	$30 \mu\text{m}$	Demagnified pixel size
CRL pre-focus	Alignment scan	Overview scan	$20 \mu\text{m}$
CRL focus	Scanning SAXS/WAXS	Scan size	$2 \mu\text{m}$
FZP	Holography, scanning	Scan size	$30 \text{nm}$
MZP	Holography, scanning	Scan size	$5 \text{nm}$

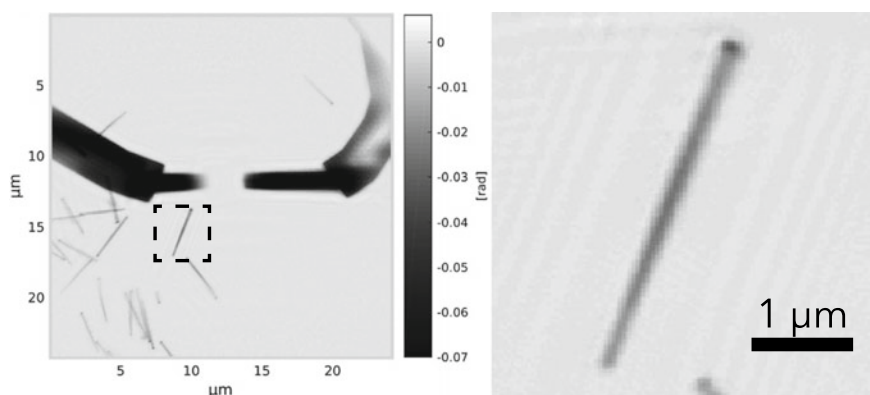


**Fig. 22.8** Phase-reconstruction from a holographic measurement on semiconductor nanowires (see Fig. 22.2). Using the relaxed averaged alternating reflection (RAAR) algorithm, quantitative phase information of the nanowires and electrical contacts can be extracted

### 22.5.3 Scanning WAXS

High X-ray energies beyond 30 keV offer long penetration lengths into bulk material, so that even hidden and buried particles can be studied. Many composite materials are crystalline, with particle sizes in the sub- $\mu\text{m}$  region; also, crystal domains within larger compounds of few hundred nm in size are common. So far, small structures can be studied ex-situ, i.e. as isolated or free-standing objects. But often, chemical and physical properties change when devices are assembled from individual components [10].

To demonstrate that MZP optics can be used in a scanning nano-WAXS setup, we have fabricated a focusing optic with unprecedented aspect ratios for hard X-ray



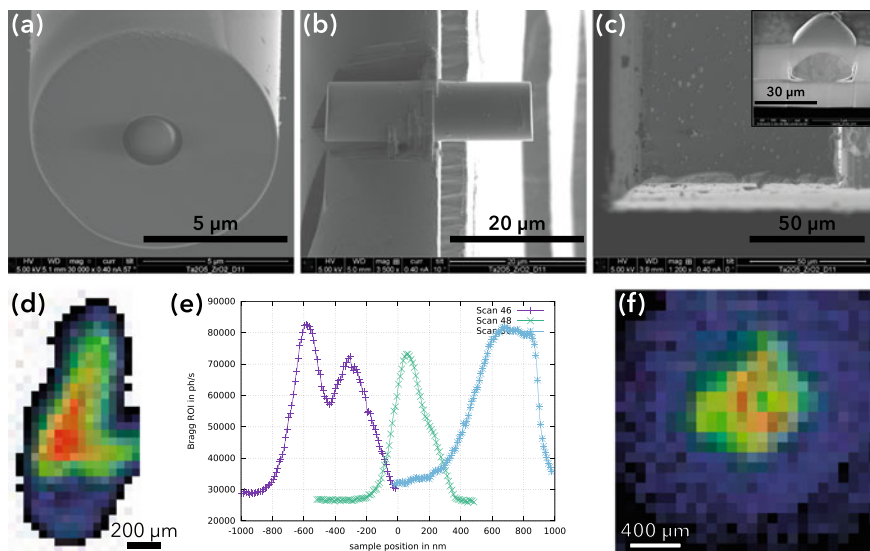


**Fig. 22.9** **a** Front SEM view of the high- $E$  MZP, showing an  $8\ \mu\text{m}$  aperture. **b** Side SEM view of the high- $E$  MZP, showing the optical thickness of  $30\ \mu\text{m}$ . **c** An imprint of Ag droplets/nanocrystals, sandwiched between two layers of  $\text{ZrO}_2$  (SEM top view). The inset shows an SEM image of one droplet after it has been exposed with FIB. **d** Spatially resolved Bragg peak intensity, measured at  $E = 60\ \text{keV}$ . **e** 1D line scans of the same droplet (shifted for clarity), showing substructure in scan 46 (purple). In case of scan 50 (light blue), the droplet serves as a knife edge with a steepness of better than  $50\ \text{nm}$ . Note that the droplet was not actually in the best focal plane of the MZP. **f** Spatially resolved Bragg peak intensity, measured at  $E = 101\ \text{keV}$

energies. SEM images of the final MZP are shown in Fig. 22.9a, b. The lens has a diameter of  $8\ \mu\text{m}$  with outer-most zones of  $10\ \text{nm}$ , and an optical thickness of  $30\ \mu\text{m}$ . This length is optimised for a phase-shifting zone plate at an X-ray energy of  $60\ \text{keV}$ .

As a test sample, Ag droplets (nano crystallites developing during the PLD process for detuned parameters) were buried within  $1.5\ \mu\text{m}$  thick layers of  $\text{ZrO}_2$  on a planar Si substrate. The typical droplet size is on the single  $\mu\text{m}$  scale. Figure 22.9c shows a top SEM view of the specimen. Although the droplets are buried, their shape and position can be seen as imprints on the surface. The inset shows an SEM image of a Ag droplet exposed with a FIB after the beamtime [10].

The experiment was performed at the high-energy station of ID31 at the ESRF (Grenoble, France). In the first user experiment with the new Laue-Laue bending monochromator, X-ray energies at  $60\ \text{keV}$  (bandwidth  $0.44\%$ ) and  $101\ \text{keV}$  (bandwidth  $0.57\%$ ) were selected from the 5th or 9th harmonic, respectively, of an in-vacuum cryo-cooled undulator with a  $14.5\ \text{mm}$  period. The X-ray beam was pre-focused by up to 288 Be lenses, in order to illuminate the MZP. The Bragg diffraction patterns were recorded with a Pilatus3 CdTe 2M detector (Dectris Inc., Baden-Daetwill, Switzerland).

The undiffracted order of the MZP illuminated basically a diluted powder of droplets and an amorphous thin Ag film. This resulted in a Debye-Scherrer ring at  $0.4 \text{ \AA}^{-1}$  or a Bragg angle of  $1.5^\circ$  at 101 keV on the detector. While the sample was raster-scanned through the MZP focus, a single Bragg peak was heavily excited above background level. Figure 22.9d shows a real-space mapping of the intensity in a single Bragg peak, showing the outline of a particular crystal grain inside one droplet. The lateral size of the grain is about 500 nm, compatible with sizes seen with the FIB.

Line scans through the intensity profile are shown in Fig. 22.9e for measurements at 60 keV, and for a different droplet (Fig. 22.9f) measured at 101 keV. The resolution has been determined to be better than 50 nm at 60 keV and even better than 40 nm at 101 keV. The full potential of the MZP focus depends of course on properly aligning the sample in the focal plane, which has not been achieved in the presented experiment. Nonetheless, the results show the feasibility of nano-focusing three-digit energies that are able to penetrate into nano-sized particles buried deeply inside bulk material [10].

#### 22.5.4 Correlative Scans

Recently, zone plate based holography was combined with scanning in both SAXS and WAXS regime. To this end, project C12 teamed up with projects B03 and B10 (Simone Techert). A sample made of amino acid crystallites (D- and L-Tryptophan) was raster scanned sequentially with a large WAXS detector (EigerX in “front position” at about 0.3 m) and then with a smaller SAXS detector (Pilatus in “rear position” at about 5.1 m). In addition, holographic datasets have been taken. Due to alignment difficulties, most scans were performed using a Fresnel Zone Plate (outermost zone width 30 nm) and Compound Refractive Lenses (focal spot size on the  $\mu\text{m}$  scale). A systematic measurement to study the growth process of such crystallites is envisioned; to spatially resolve the real-space sub-structure, a Multilayer Zone Plate will be used.

This setup combines certain strengths of the different modalities. Holography is—in principle—a full-field technique; here it is combined with small scans of the sample to implement the “software OSA”. With the FZP, large overview images at moderate resolution can be obtained. Changing to the MZP optic, a zoom-in capability with a field of view slightly larger than the crystallites and at few nanometre spatial resolution become possible. The fundamental contrast mechanism is the phase shift due to the electron density of the specimens.

Scanning SAXS, on the other hand, is sensitive to surfaces and especially morphology; since length scales of up to 100 nm can be probed, it is beneficial to use the CRL beam. With scanning WAXS, then, it becomes possible to distinguish the crystalline grains within the sample.

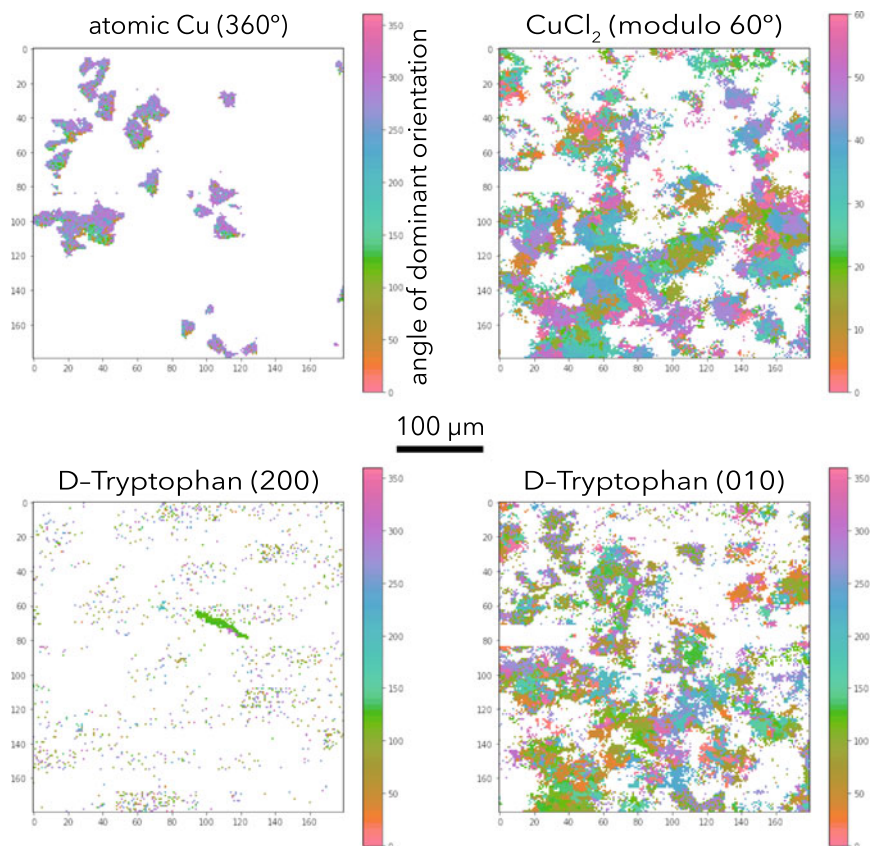


**Fig. 22.10** Dominant crystallite orientations mapped into real-space, for **a** pure Cu, **b** CuCl, **c** D-Tryptophan (200) and **d** D-Tryptophan (010) lattices

From preliminary scanning-WAXS measurements, the dominant crystallite orientations can be mapped into real-space images. Figure 22.10 shows these dominant orientations for (b) CuCl, (c) D-Tryptophan (200), and (d) D-Tryptophan (010).

A detailed analysis to study correlations in reciprocal and real-space is still on-going.

## 22.6 Summary

During the second funding period, a collaboration of projects C01 and C04 have demonstrated the first two-dimensional 5 nm X-ray focus. Building on this, project C12 has further developed hard X-ray imaging in different areas. Together with C01, the GINIX setup at the P10 beamline (DESY Hamburg) has been optimised in

terms of motorisation, reducing of vibrations / drift, automated data handling, and in the end image resolution. During a beamtime at the ESRF (Grenoble, France), high energy X-rays of 101 keV could be used to localise buried nano-crystallites at a spatial resolution better than 50 nm. In a joint work with projects B03/B10, the possibility of imaging and crystallite mapping has been successfully explored on organic matter. A full analysis on the complex structures of the Tryptophan sample is, however, beyond the scope of project C12.

With the retirement of one of the principal investigators (H.U.K.), the deposition process and optimisation thereof has been paused; however, new MZPs have successfully been cut out off existing coated wires for new experiments.

Due to rapidly increasing amounts of data from scanning experiments, processing and analysis had stagnated for a while; with the Heinzelnächten system, a dedicated analysis platform for scanning SAXS data was commissioned and has served different projects within this collaborative research centre.

## References

1. Reese, M.: *Fabrication of Soft X-ray Optics and their Characterisation with Laboratory and Synchrotron Sources*. Universitätsverlag Göttingen (2011)
2. Reese, M., Schäfer, B., Großmann, P., Bayer, A., Mann, K., Liese, T., Krebs, H.: Submicron focusing of xuv radiation from a laser plasma source using a multilayer laue lens. *Appl. Phys. A Mater. Process.* **102**, 85–90 (2010)
3. Ruhlandt, A., Liese, T., Radisch, V., Krüger, S.P., Osterhoff, M., Giewekemeyer, K., Krebs, H.U., Salditt, T.: A combined kirkpatrick-baez mirror and multilayer lens for sub-10 nm X-ray focusing. *AIP Adv.* **2**, 012,175 (2012). <https://doi.org/10.1063/1.3698119>
4. Döring, F., Robisch, A.L., Eberl, C., Osterhoff, M., Ruhlandt, A., Liese, T., Schlenkrich, F., Hoffmann, S., Bartels, M., Salditt, T., Krebs, H.U.: Sub-5 nm hard X-ray point focusing by a combined kirkpatrick-baez mirror and multilayer zone plate. *Opt. Express* **21**, 19311–19323 (2013). <https://doi.org/10.1364/OE.21.019311>
5. Osterhoff, M., Eberl, C., Döring, F., Wilke, R., Wallentin, J., Krebs, H., Sprung, M., Salditt, T.: Towards multi-order hard x-ray imaging with multilayer zone plates. *J. Appl. Crystallogr.* **48**, 116–124 (2015). <https://doi.org/10.1107/S1600576714026016>
6. Wallentin, J., Anttu, N., Asoli, D., Huffman, M., Åberg, I., Magnusson, M.H., Siefer, G., Fuss-Kailuweit, P., Dimroth, F., Witzigmann, B., Xu, H.Q., Samuelson, L., Deppert, K., Borgström, M.T.: Inp nanowire array solar cellsachieving 13.8% efficiency byexceeding the ray optics limit. *Science* **339**, 1057–1060 (2013). <https://doi.org/10.1126/science.1230969>
7. Eberl, C., Döring, F., Liese, T., Schlenkrich, F., Roos, B., Hahn, M., Hoinkes, T., Rauschenbeutel, A., Osterhoff, M., Salditt, T., Krebs, H.U.: Fabrication of laser deposited high-quality multilayer zone plates for hard x-ray nanofocusing. *Appl. Surf. Sci.* **307**, 638–644 (2014). <https://doi.org/10.1016/j.apsusc.2014.04.089>
8. Eberl, C., Liese, T., Schlenkrich, F., Döring, F., Hofsäss, H., Krebs, H.U.: Enhanced resputtering and asymmetric interface mixing in w/si multilayers. *Appl. Phys. A* **111**, 431 (2013)
9. Eberl, C., Osterhoff, M., Döring, F., Krebs, H.U.: Mzp design and fabrication for efficient hard x-ray nano-focusing and imaging. In: *Proceedings of SPIE Advances in X-Ray/EUV Optics and Components X* **958**, 808 (2015). <https://doi.org/10.1117/12.2187788>
10. Osterhoff, M., Soltau, J., Eberl, C., Krebs, H.U.: Ultra-high-aspect multilayer zone plates for even higher x-ray energies. In: *Proceedings of SPIE Advances in X-Ray/EUV Optics and Components XII*, vol. 10386, 1038,608 (2017). <https://doi.org/10.1117/12.2271139>
11. Warken, F., Rauschenbeutel, A., Bartholomäus, T.: Fiber pulling profits from precise positioning. *Photonics Spectra* **42**, 73–75 (2008)

12. Salditt, T., Osterhoff, M., Krenkel, M., Wilke, R., Priebe, M., Bartels, M., Kalbfleisch, S., Sprung, M.: Compound focusing mirror and x-ray waveguide optics for coherent imaging and nano-diffraction by Markus Osterhoff. *J. Synchr. Radiat.* **22**, 867–878 (2015). <https://doi.org/10.1107/S1600577515007742>
13. Osterhoff, M., Eberl, C., Soltau, J., Krebs, H.: Preparing for hard x-ray microscopy with multilayer zone plates. *J Phys Conf Ser* **849**, 012,049 (2016). <https://doi.org/10.1088/1742-6596/849/1/012049>
14. Osterhoff, M., Soltau, J., Eberl, C., Krebs, H.U.: Faster scanning and higher resolution: new setup for multilayer zone plate imaging. In: *Proceedings of SPIE X-ray Nanoimaging: Instruments and Methods III*, vol. 10389, 103,890T (2017). <https://doi.org/10.1117/12.2271141>
15. Dectris Award Winner Heinzelnännchen. <https://www.dectris.com/company/news/newsroom/news-details/dectris-award-winner-heinzelnannchen-analyse-x-ray-images>, 27 Mar (2018)
16. Osterhoff, M., Goeman, J., Salditt, T., Köster, S.: Stxm analysis: preparing to go live @ 750 hz. In: *AIP Conference Proceedings*, vol. 2054, 060,075 (2019). <https://doi.org/10.1063/1.5084706>
17. Bernhardt, M., Nicolas, J.D., Eckermann, M., Eltzner, B., Rehfeldt, F., Salditt, T.: Anisotropic x-ray scattering and orientation fields in cardiac tissue cells. *New J. Phys.* **19**, 013,012 (2016). <https://doi.org/10.1088/1367-2630/19/1/013012>
18. Feigin, L., Svergun, D.: *Structure Analysis by Small-Angle X-Ray and Neutron Scattering*. Springer (1987)
19. Hémmontot, C., Köster, S.: Imaging of biological materials and cells by x-ray scattering and diffractions. *ACS Nano* **11**, 8542–8559 (2017). <https://doi.org/10.1021/acs.nano.7b03447>
20. Nicolas, J.D., Bernhardt, M., Schlick, S.F., Tiburcy, M., Zimmermann, W.H., Khan, A., Markus, A., Alves, F., Toischer, K., Salditt, T.: X-ray diffraction imaging of cardiac cells and tissue. *Progress Biophys. Mol. Biol.* (In press 2019). <https://doi.org/10.1016/j.pbiomolbio.2018.05.012>
21. Priebe, M., Bernhardt, M., Blum, C., Tarantola, M., Bodenschatz, E., Salditt, T.: Scanning x-ray nanodiffraction on dictyostelium discoideum. *Biophys J.* **107**, 2662–2673 (2014). <https://doi.org/10.1016/j.bpj.2014.10.027>
22. Weinhausen, B., Nolting, J.F., Olendrowitz, C., Langfahl-Klabes, J., Reynolds, M., Salditt, T., Köster, S.: X-ray nano-diffraction on cytoskeletal networks. *New J. Phys.* **14**, 085,013 (2012). <https://doi.org/10.1088/1367-2630/14/8/085013>

**Open Access** This chapter is licensed under the terms of the Creative Commons Attribution 4.0 International License (<http://creativecommons.org/licenses/by/4.0/>), which permits use, sharing, adaptation, distribution and reproduction in any medium or format, as long as you give appropriate credit to the original author(s) and the source, provide a link to the Creative Commons license and indicate if changes were made.

The images or other third party material in this chapter are included in the chapter's Creative Commons license, unless indicated otherwise in a credit line to the material. If material is not included in the chapter's Creative Commons license and your intended use is not permitted by statutory regulation or exceeds the permitted use, you will need to obtain permission directly from the copyright holder.

